CHINESE JOURNAL OF PHYSICS VOL. 45 , NO. 4 AUGUST 2007

Review

Surface One-Dimensional Structures

Shuji Hasegawa*

Department of Physics, University of Tokyo,
7-3-1 Hongo, Bunkyo-ku, Tokyo 113-0033, Japan
(Received April 25,2007)

One-dimensional (1D) metallic structures, self-assembled on semiconductor surfaces (surface superstructures) are discussed, showing the characteristic atomic arrangements, band dispersions, Fermi surfaces, phase transitions, and electronic transport properties. Experimental techniques for directly probing the structures and properties, such as four-tip scanning tunneling microscopy, the monolithic microscopic four-point probe method, and angle-resolved photoemission spectroscopy, are also introduced. Owing to the good controllability of the surface structures and the direct accessibility by the experimental techniques, the surface-1D systems are now a new platform for nanometer-scale 1D physics.

PACS numbers: 73.63.-b, 68.65.-k, 73.20.-r

I. INTRODUCTION

One-dimensional (1D) structures, in which electrons are confined to move freely only in one direction, are realized in various material systems, such as quantum/nano wires, atomic/molecular chains, nanotubes, quantum edge states, and highly anisotropic (in)organic crystals. Regular arrays of atomic chains and nanowires, self-assembled on crystal surfaces (1D surface superstructures), are recent examples of such 1D structures (though there is some inter-chain interaction, resulting in *quasi*-1D). Various kinds of exotic physics are expected in such (quasi-)1D systems as described below, some of which are directly observed by some experimental techniques.

Why are the 1D structures so interesting in physics? From the theoretical point of view, 1D systems are relatively easy to solve compared with two-dimensional (2D) and three-dimensional (3D) systems; analytical solutions including strong electron-correlation effects are sometimes obtained only for 1D systems [1] (though it is quite difficult to realize real 1D systems experimentally). The 1D electron systems are noted for having the following interesting features.

1. **Density of states, band dispersion, and Fermi surfaces**. The density of states

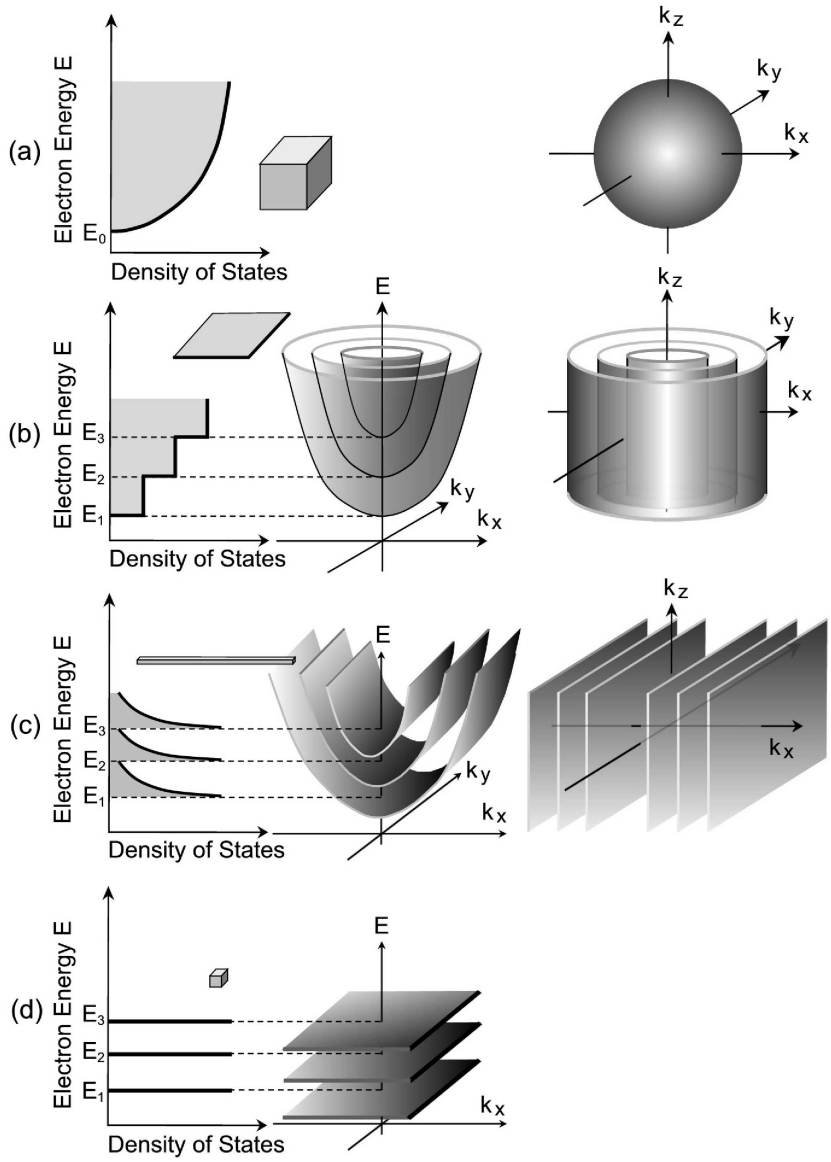

FIG. 1: Schematic illustrations of the density of states (left column), band dispersion (center column), and Fermi surfaces (right column) of (a) 3D, (b) 2D, (c) 1D, and (d) 0D free-electron systems.

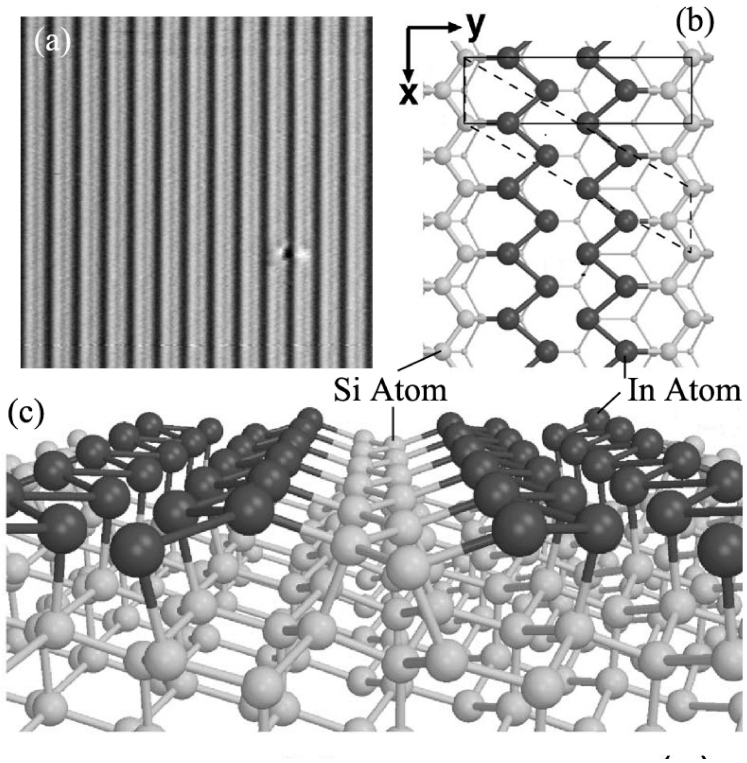

FIG. 2: Si(111)-4 × 1-In surface superstructure. (a) Its STM image at room temperature. (b) Atomic structure model in plan view, and (c) in ball-and-stick model, reproduced from Ref. [15].

(DOS) of free electron systems in 0D, 1D, 2D, and 3D are written as

$$0D: \quad D(E) = 2\sum_n \delta(E - E_n) \tag{1}$$

$$1D: \quad D(E) = 2\left(\frac{m^*}{2\hbar^2\pi^2}\right)\sum_n \frac{H(E - E_n)}{\sqrt{|E - E_n|}}, \tag{2}$$

$$2D: \quad D(E) = \frac{m^*}{\pi\hbar^2} \cdot \sum_n H(E - E_n), \tag{3}$$

$$3D: \quad D(E) = \frac{1}{2\pi^2}\left(\frac{2m^*}{\hbar^2}\right)^{3/2}\sqrt{E}, \tag{4}$$

where $H(x)$ is Heaviside step function ($H(x) = 0$ $(x \leq 0)$, $= 1(x > 0)$), and the effective mass m^* is assumed to be isotropic for simplicity [2]. The DOS shapes are illustrated in Fig. 1. The DOS in 3D changes smoothly with energy, while it changes

rapidly and significantly with energy as the dimension is lowered. The DOS in 1D systems diverges at the bottoms of bands, which is never seen in 2D and 3D systems. This van Hove singularity raises some interesting phenomena in optical, transport, and magnetic properties. Isotropic 2D free-electron systems have parabolic sub-bands in any direction and circular Fermi surfaces, as shown in (b). Strict 1D free-electron systems have parabolic sub-bands only in one direction (the k_x direction), while the sub-bands do not show any dispersion in the perpendicular direction (the k_y direction) as shown in (c). Its Fermi surface is composed of straight lines. The 0D systems such as quantum dots have discrete energy levels which do not show any dispersion in k-space, as shown in (d). The 1D systems are characterized by highly anisotropic properties originated by the anisotropic band dispersion and Fermi surface.

2. **Ballistic transport and conductance quantization**. When the carriers flow through a 1D system without scattering, it is called ballistic transport. The conductance in this case is quantized in units of $2e^2/h$, the Landauer formula [3]. Depending on the width of the 1D systems, which determines the number of sub-bands in the electronic band structure, the conductance is a multiple of $2e^2/h$. Since this unit is written in terms of universal constants only, it is not dependent on the material. This is one of the most striking results for 1D systems. For ballistic transport in 2D and 3D, in contrast, the conductivity values are written including the Fermi wavenumber, which is material-dependent [4]

3. **Carrier mobility**. It is expected that the mobility of carriers in 1D systems should be higher than that in higher dimensions, because of the reduction of the carrier scattering probability [5]; only 180°-scattering is allowed in 1D. However, influence on carrier scattering by defects and impurities in 1D systems is much more serious than in 2D and 3D systems, because the carriers cannot avoid the scatterers in 1D and the screening of scatterers is less sufficient there. This actually reduces the carrier mobility in many cases.

4. **Fluctuation, instability, localization**. 1D metals have large fluctuations and are essentially unstable (Peierls instability) at low enough temperatures because of Fermi surface nesting [6]. The Lindhard response function diverges at the wavenumber $k = 2k_F$, where k_F is the Fermi wavenumber. This means that infinitesimal stimulation having a Fourier component at $2k_F$ causes some finite response in 1D systems, that is, an instability. Due to electron-phonon coupling, this instability inevitably induces lattice distortions and energy-gap opening at the Fermi level. Such an instability raises charge-density waves (CDW), and the system goes into an insulating phase. Such a metal-insulator transition occurs by cooling in many 1D systems. Insulating phases are frequently observed at low temperature in reduced dimension due to carrier localization, which originates from random potentials caused by defects and impurities. Many of the 1D systems will be insulating at the ground state due to these effects.

5. **Electron correlation**. Electrons inevitably interact with each other strongly in 1D systems, because they cannot avoid each other when their motion is restricted only in one direction; their wavefunctions overlap and the interaction is maximized. As a result, the Fermi-liquid picture, in which the electron motion near the Fermi level is assumed not to be affected by Coulomb interaction with other electrons, is not applicable any more to such strict 1D systems. Instead, the Tomonaga-Luttinger-liquid concept works where the single-electron picture is replaced by collective excitations. Carbon nanotubes and semiconductor quantum wires are shown to exhibit the Tomonaga-Luttinger-liquid features in photoemission spectra and the temperature dependence of electrical conductivity [7, 8], and there are many reports and discussion about other material systems. At the moment, however, there is no definite confirmation of the Tomonaga-Luttinger-liquid features in (quasi-)1D surface superstructures. Inter-chain interaction, electron-phonon coupling and charge-density wave formation, and other practical factors prevent the observation. Looking for the Tomonaga-Luttinger-liquid behavior is one of the most interesting topics in surface physics.

6. **Magnetic moment**. When a magnetic atom has fewer neighbors with ferromagnetic coupling, the orbital magnetic moment is enhanced. Furthermore, in general, larger anisotropic magnetic energy is expected in a 1D magnetic structure. Therefore, 1D systems have a possibility to realize magnetic systems with large magnetization. Actually, chains of magnetic atoms aligned at step edges on a crystal surface are shown to have a larger magnetic moment than that in a 3D crystal of the material [9].

One of the ways to fabricate 1D systems with good controllability is to confine one-dimensionally the 2D electron gas (2DEG) formed at semiconductor hetero-junctions. By applying an electric field with gate electrodes that are micro-fabricated on top of the 2DEG, electrons can be confined in any designed regions, and the size of the regions can be as small as the wavelength of the conduction electrons. The advanced technology in semiconductor micro-fabrication enables us to prepare samples of such designed quantum systems including 1D structures [5, 10].

Self-assembled surface superstructures on crystals are another type of artificial quantum structure which can have some interesting features different from the previous semiconductor quantum structures. Not only the quantum confinement of the electrons, but also the details of the atomic arrangement affect the electronic structures and resulting transport properties much more explicitly. The surface electronic states are sometimes formed within the energy gap in the bulk band structure of the substrate crystal, which means that the surface states are electronically isolated from the substrate. Carriers in the surface states, therefore, can flow through them (surface-state conduction), while only inelastic scattering with large energy transfer makes the carriers leak into the substrate.

Various kinds of adsorbate-induced surface superstructures with around monatomic layer adsorption are known which show features of, e.g., a 2D metal, a quasi-1D metal, a 2D Mott insulator, a Peierls insulator, and a localization insulator. Tiny amounts of

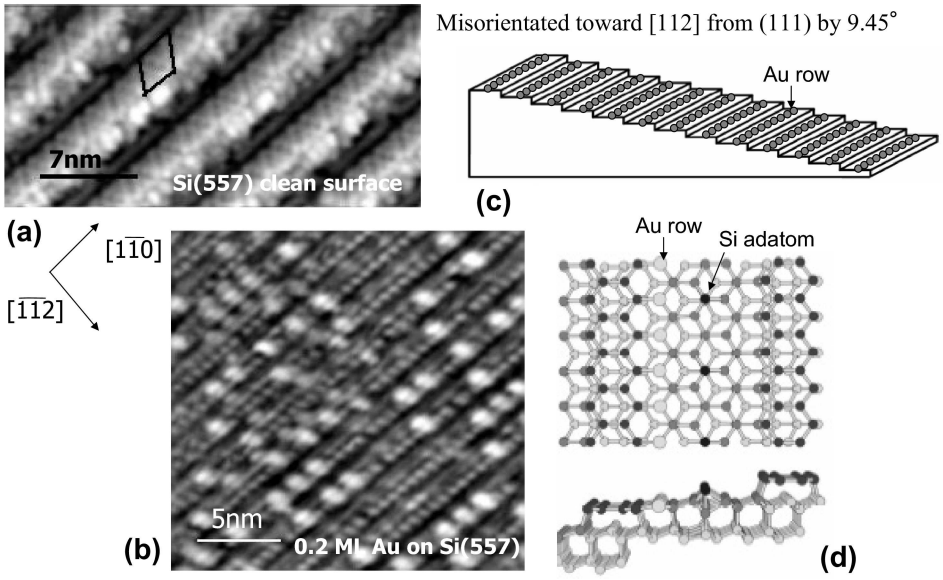

FIG. 3: Si(557)-Au surface. STM images of clean Si(557) surface (a) and of Au of 0.2 ML adsorbed Si(557) surface (b) [18]. (c) Schematic illustration of the vicinal surface, and (d) a model of the atomic structure, reproduced from Ref. [19].

adatoms less than one atomic layer sometimes drastically change the band structure, the Fermi surface, and the electrical conductivity. Phase transitions characteristic of surface superstructures also definitely affect the transport properties. Therefore, the surface-state electrical conduction, which is the conduction through one or two topmost atomic layers of crystal surfaces, should produce rich transport physics.

In this review paper, I introduce the atomic structures, electronic band structures, and transport properties of some well-studied, but not yet fully understood, examples of quasi-1D surface structures formed on silicon crystals by metal adsorptions, Si(111)-4 × 1-In, Si(557)-Au, and $CoSi_2$ nanowires on Si(110). Scanning tunneling microscopy (STM), angle-resolved photoemission spectroscopy (ARPES), four-tip STM and monolithic micro-four-point probe methods are employed for analyzing the atomic/electronic structures and transport properties.

II. ATOMIC STRUCTURE

When one monolayer (ML) of indium atoms adsorb on a Si(111) surface at around 400°C, the Si(111)-4 × 1-In surface superstructure is formed. As shown in Figs. 2(b)(c), its atomic arrangement is a massive array of metallic quantum wires composed of four lines of In atom chains running along the [10$\bar{1}$] direction, each wire being separated by a Si-atom zigzag chain in between the metallic wires. Bright stripes in the STM image (a)

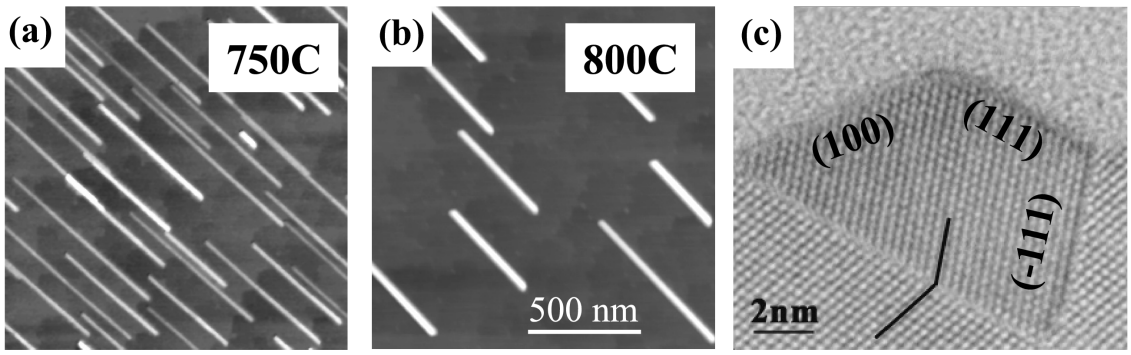

FIG. 4: Self-assembled $CoSi_2$ nanowires formed on a Si(110) substrate, reproduced from Refs. [21, 22]. As the substrate temperature is higher at the Co deposition, the wires becomes shorter and wider, as shown in (a) and (b). (c) A cross-sectional transmission electron micrograph.

correspond to the four In atomic chains, and dark trenches are Si chains. This structure was determined first by x-ray diffraction analysis [11], followed by electron diffraction [12, 13] and also by first-principle calculations [14, 15]. As imagined from this atomic arrangement, it has a metallic nature along the In chains, while having an insulating character across the chains. This surface superstructure is contrasted to the Si(111)$\sqrt{3} \times \sqrt{3}$-Ag surface having an isotropic 2D metallic surface state [16, 17].

Another example of quasi-1D metallic surfaces is shown in Fig. 3, where Au atomic chains are formed on a stepped Si surface, Si(557). Figure 3(a) is a STM image of a clean Si(557) surface, which is composed of regular arrays of narrow terraces having the 7×7 structure and triple-atomic steps. When Au of 0.2 ML is deposited on this surface at elevated temperatures, the triple-atomic-step structure changes into a single-atomic-step one as shown in Fig. 3(b) [18]. A single Au atomic chain is formed on each terrace as shown in (c) and (d). The model of atomic structure (d) is proposed based on X-ray diffraction analysis [19]. On this regular atomic structure, the STM image (b) shows bright protrusions arranged irregularly. These protrusions are inevitable; we cannot remove them by controlling the sample preparation conditions, although the density can vary to some extent. The irregular protrusions play an important role in electrical conduction, as described in Section 4.

Figure 4 shows $CoSi_2$ nanowires formed on a Si(110) surface. These are self-assembled just by Co deposition on the Si substrate at around 750°C because of anisotropy in the substrate surface structure [20, 21]. The nanowires are well-separated from each other, so that any inter-wire interaction does not work. The wires are perfectly single-crystalline, and are half embedded in the substrate, as shown by a cross-sectional transmission electron micrograph Fig. 3(c) [22].

A kind of ultimate atomic chain structure is shown in Fig. 5. Monatomic chains of indium are self-assembled on a Si(001) surface [23]. The chains are aligned perpendicular to the dimer rows on the substrate, and well separated from each other. The transport

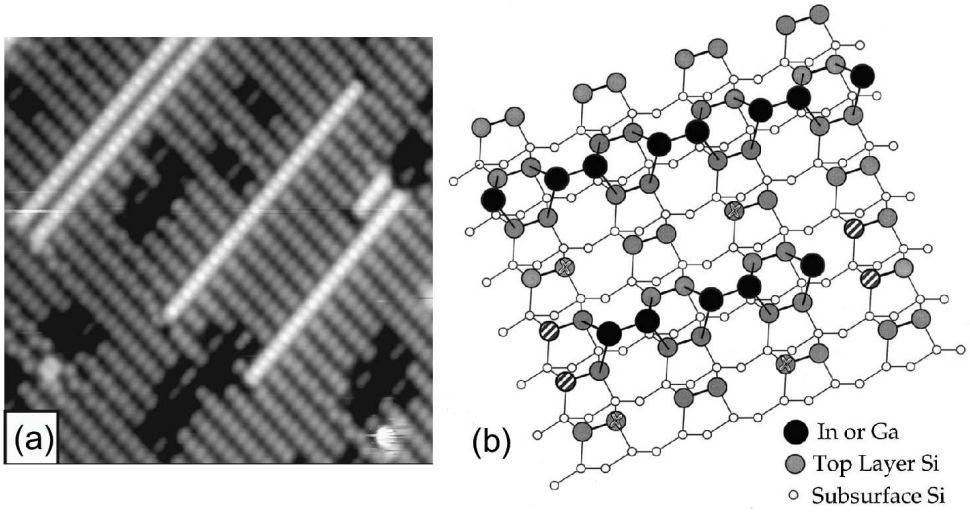

FIG. 5: (a) STM image of In atomic chains on a Si(001) surface, and (b) a model of its atomic arrangement, reproduced from Ref. [23].

properties of the individual chains are very interesting to measure, which has, however, not yet been done for lack of experimental techniques.

As shown here, there are various kinds of 1D structures which are self-assembled on Si crystal surfaces and are good samples for exploring 1D physics at nanometer scale, because the structures are well-defined and many sophisticated surface-science techniques are applicable for the investigation.

III. ELECTRONIC STRUCTURE

Angle-resolved photoemission spectroscopy (ARPES) measurements reveal that some of these (quasi-)1D surface structures have actually highly anisotropic metallic surface states. Figure 6(a) shows the band dispersion along the In chains (k_x direction//$[10\overline{1}]_{\rm Si}$) taken from the Si(111)-4 × 1-In surface [24]. We recognize clearly three parabolic bands, m1, m2, and m3, crossing the Fermi level (E_F) [25]. These surface-state bands, however, do no show significant dispersion in the perpendicular direction (k_y direction), as shown by a three-dimensional illustration of band dispersion in (d). This means that electrons move freely only along the In chains, while it is hard for electrons to hop to the neighboring chains. ARPES measurements enables us to map out the Fermi surface as shown in (b) and illustrated in (c). The three bands make almost straight Fermi lines although they are slightly wavy. Therefore the energy dispersion and Fermi surface are just as illustrated in Fig. 1(c). This is a quasi-1D metal.

There is one more interesting thing which is characteristic of the quasi-1D metallic

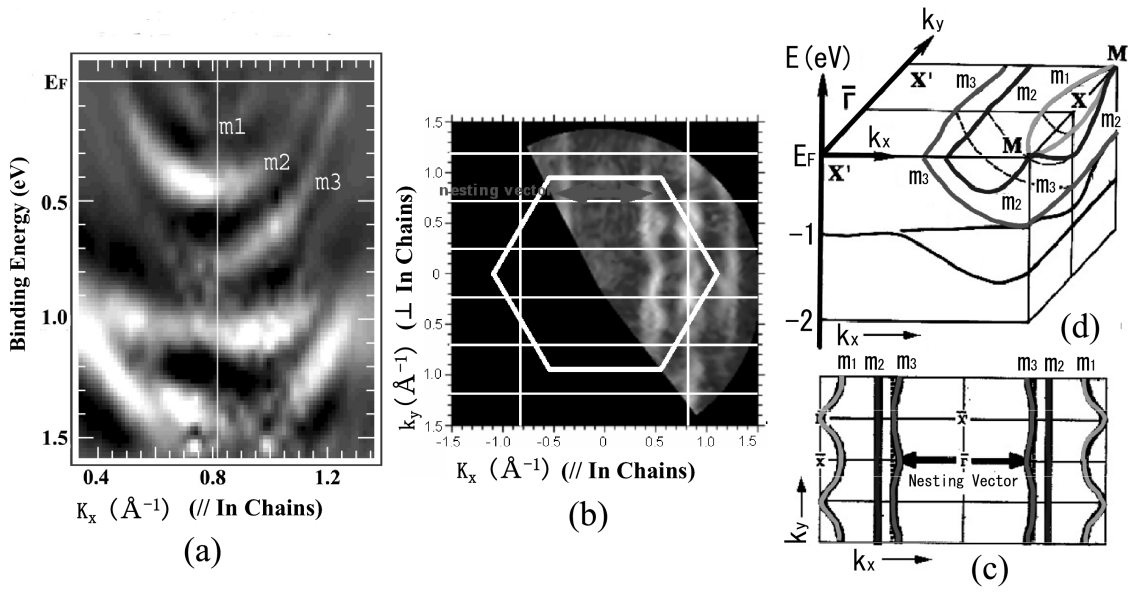

FIG. 6: The electronic state of a Si(111)-4 × 1-In surface superstructure. (a) Band dispersion along the In atomic chains, constructed from angle-resolved photoemission spectra [24]. (b) Fermi surface map, and (c) its schematic [26]. (d) Three-dimensional illustration of the band dispersion. The binding energy E is a function of the components of the wave vector, k_x along the In chains and k_y across the chains.

systems. The almost straight lines in the Fermi surface (Figs. 6(b)(c)) satisfy the nesting condition, meaning that some portions in the Fermi surface can be overlapped with other portions by a parallel translation in k-space. The direction and distance of the translation is indicated by the nesting vector. Straight Fermi lines of 1D metal systems always satisfy this condition. If this condition is satisfied, the system responds very sensitively to any stimulation having the Fourier component equal to the nesting vector. This leads to a static distortion of the lattice accompanied by charge-density modulation, i.e., a charge-density-wave (CDW) transition. Actually the 4×1-In surface is known to reveal a phase transition by cooling; the 4×1 changes to a $8 \times' 2'$ superstructure around 130 K, as shown in the STM images of Figs. 7(e)(f) [26]. This periodicity doubling along the In chains corresponds to the nesting vector due to the nearly half-filled bands m2 and m3 in Fig. 6; the Fermi lines bisect the surface Brillouin zone. Half-order reflections emerge in the electron diffraction pattern, meaning that the lattice also distorts to form a double periodicity. In this way, both the lattice distortion and charge modulation have the same periodicity due to electron-phonon coupling. The STM image Fig. 7(f) shows clear double-periodicity modulation in many In chains, while some chains do not show clear CDW modulation. This is due to CDW fluctuations. Each stripe appears to behave independently, which is due to the very small inter-chain coupling. Due to the CDW transition (Peierls transition), an energy gap opens at E_F, as shown in Figs. 7(a)(b), and the surface becomes insulating. This is actually shown

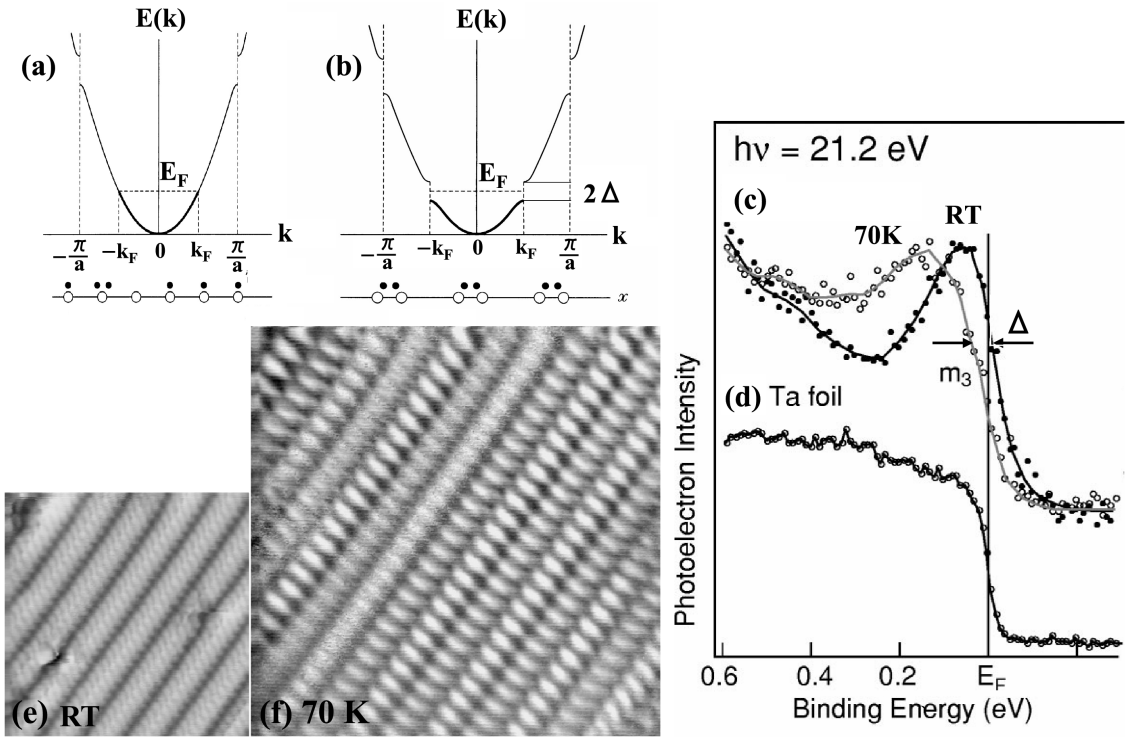

FIG. 7: The Peierls transition in a Si(111)-4 × 1-In surface superstructure. Schematics of band dispersion and atomic arrangement of one-dimensional metal (a) in the metallic phase at higher temperature and (b) in the charge-density-wave phase at lower temperature. (c) Photoemission spectra from the 4 × 1-In surface at RT and 70 K, reproduced from Ref. [27]. (d) Photoemission spectrum from a Ta clamp to determine the Fermi level. (e) STM images at RT and (f) at 70 K [26].

by the photoemission spectra (c); the leading edge at E_F shifts to the left at 70 K compared with the room-temperature spectrum [27]. This metal-insulator transition accompanied by CDW formation results in a drastic decrease in surface conductivity as described in Section 4 [28].

In addition to the usual CDW transition picture described above, a theory has proposed a different picture for the $4 \times 1 \rightarrow 8 \times' 2'$ phase transition by stressing an importance of fluctuations [31]. According to the theory, the high-temperature phase (4×1) is a kind of time-averaged structure of the fluctuation among four energy-degenerate 4×2 structures that are building blocks of the low-temperature phase ($8 \times' 2'$). The phase transition by cooling is understood as a freezing of the fluctuation. The change of electronic structure is explained by the transient structures during the fluctuation. However, it is not clear whether this picture of an order-disorder type phase transition is compatible with the scenario of the CDW transition described before [29, 30].

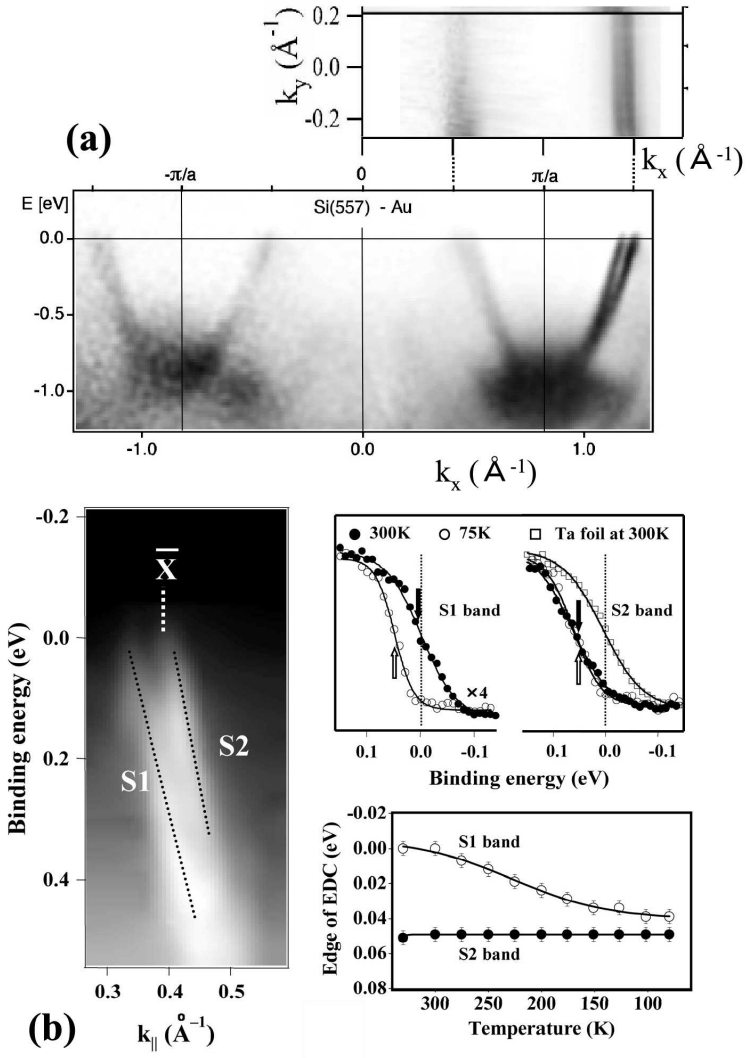

FIG. 8: (a) The band dispersion and Fermi surface of a Si(557)-Au surface, reproduced from Ref. [32]. (b) Energy-gap opening in the S1 band at E_F, reproduced from Ref. [33].

The Au-covered Si(557) surface also has a similar quasi-1D metallic band structure. It has parabolic bands crossing E_F along the Au chains (k_x direction) as shown in Fig. 8(a) [32], and the Fermi surface is almost straight. If one looks at the diagrams carefully, one may notice that the parabolic bands are actually a doublet. They are called the S1 and S2 bands, as shown in (b) [33]. This doublet of bands is proposed to be spin-split bands due to the Rashba effect in surface states [34]. According to temperature-variable photoemission spectroscopy measurements [33], however, the two bands have a different temperature dependence as shown in Fig. 8(b); one of the bands (S1) is metallic at room

temperature, while the other one (S2) already has an energy gap at room temperature. By cooling, an energy gap opens gradually for the S1 band, which corresponds to a Peierls transition. This result is inconsistent with the picture of spin-split bands mentioned above, because both bands should have the same nature and same temperature dependence if they are spin-split bands. Under the circumstances, the character of the doublet bands is not yet fully understood.

Both Si(111)-4 × 1-In and Si(557)-Au surfaces exhibit clear metallic edges at E_F in photoemission spectra at least at room temperature, as shown in Figs. 6 and 8. This means that these quasi-1D metallic systems are Fermi liquids, not Tomonaga-Luttinger liquids, because the spectral intensity $I(E)$ near E_F should be described by a power law $I(E) \propto E^{\alpha}$ if the system is a Tomonaga-Luttinger liquid [7], which is not the case for both surfaces. With cooling, the systems show a gap-opening at E_F due to the Peierls instability, which prevents us from observing the Tomonaga-Luttinger liquid behavior. Historically, the Si(557)-Au surface was proposed to be a Tomonaga-Luttinger liquid based on ARPES measurements showing two bands corresponding to spinon and holon bands, i.e., a spin-charge-separation phenomenon, which is characteristic of Tomonaga-Luttinger liquids [35]. But the following experiments denied it by showing that the two bands split at E_F, which is incompatible with the assignment to a spinon-holon pair in a Tomonoga-Luttinger liquid [36].

IV. ELECTRONIC TRANSPORT

In order to measure the electrical conductivity of these surface-1D structures, we need microscopic four-point probes (4PP) combined with some microscope for positioning the probes correctly on the sample surface. Two of the four probes are the source and drain for measuring current, and the other two probes are for measuring the voltage drop caused by the current. By this four-point probe configuration, the contact resistance between the probes and sample is avoided. We have developed two types of microscopic four-point probes (μ4PP) in which the probe spacing is from one hundred nanometer up to several tens of microns, i.e., four-tip STM and monolithic micro-four-point probes, as shown in Figs. 9 and 10, respectively.

Figure 9 shows a series of scanning electron micrographs (SEM) of the four tips arranged in various configurations in our home-made four-tip STM [37–39]. The tips are chemically etched W wires. The probe spacing can be changed from 1 mm to ca. 200 nm in Figs. 9(a)-(d). They can be arranged on a line equidistantly (linear μ4PP method) in arbitrary directions on the sample surface (e), or in a square arrangement (square-μ4PP method) (f) on the sample surface. The square can be rotated with respect to the sample surface (rotational square μ4PP method) by re-positioning each tip [39]. This is useful to measure anisotropic conductivity as described below. We have recently developed a new four-tip STM which enables variation in the temperature of the sample and tips [40].

This apparatus enables the usual STM operation with atomic resolution by each tip independently, and also 4PP conductivity measurements with various probe arrangements

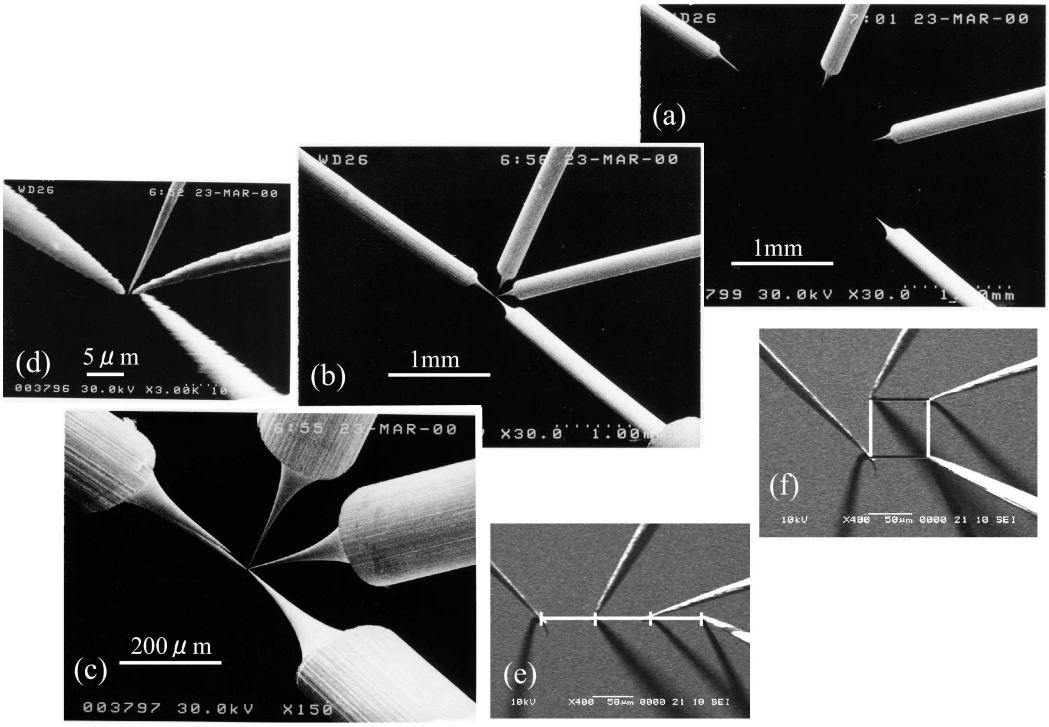

FIG. 9: SEM images of the four W tips of a four-tip STM operated in UHV. (a)-(d) The tip spacing can be changed from the millimeter to the sub-micrometer range [38]. The four tips are aligned (e) on a line with equidistance and (f) in a square arrangement [39].

and spacing as shown in Fig. 9. The four tips are made to approach the sample surface simultaneously with feedback control by tunnel current detection. After that, the tips are brought into direct contact with the sample surface, and then the 4PP conductivity measurement is performed. The pre-amplifier is switched from the tunnel-current mode to the 4PP conductivity measurement mode, in which any two tips act as current probes and other two are voltage probes. The newly developed control system enables automatic positioning of the four tips by detecting the position of each tip in an absorption-current image with the SEM electron beam [41]. The other method for navigating the two STM tips is developed by using a special sample [42].

Next I introduce another type of μ4PP method. Figure 10(a) shows a scanning electron micrograph of a chip for a monolithic μ4PP, which is produced by using silicon micro-fabrication technology [43], and is now commercially available [44]. The technique is similar to that for producing the cantilevers of atomic force microscopy. One can choose the probe spacing ranging from 2 μm to 100 μm, while probes of several hundred nm spacing are under development. The substrate is an oxide-covered silicon crystal, on which a metal layer is deposited on selected areas to make conductive paths. The metal layer

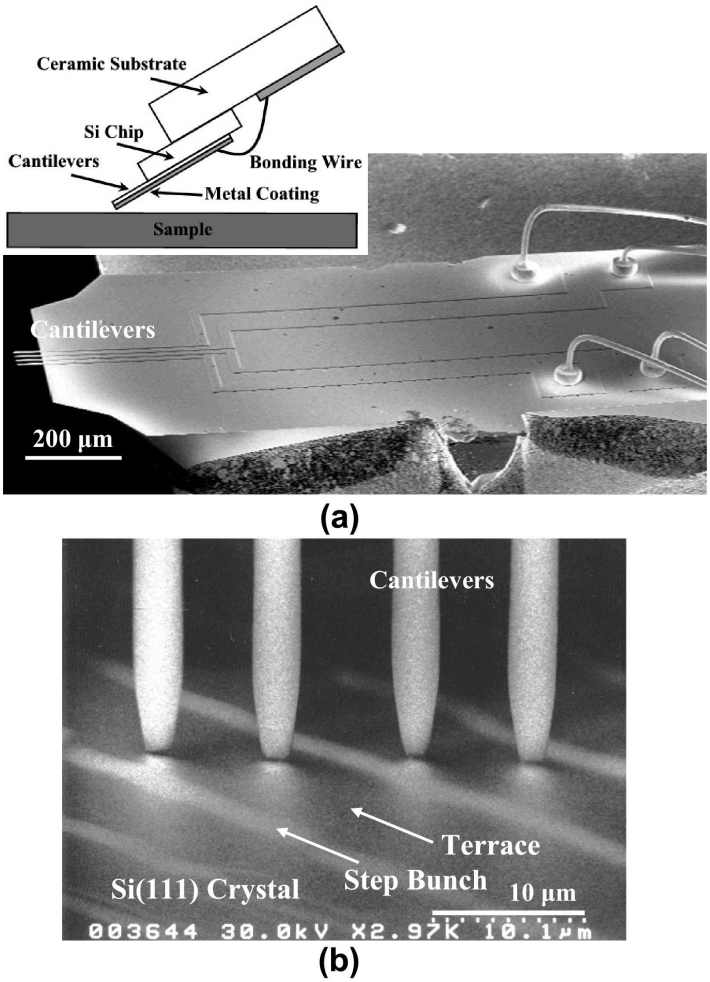

FIG. 10: A monolithic micro-four-point probe. (a) A SEM image of the chip. The inset shows a side view of the probe contacting a sample surface. (b) A grazing-incidence SEM image of a micro-four-point probe (probe spacing being 8 μm), contacting a sample (Si(111)-7 $\times$ 7 clean surface) in UHV during a measurement of conductance [46].

covers the very end of four cantilevers so that they can make direct contact to the sample surface. The angle between the cantilever and sample surface is about 30°as shown by the inset in Fig. 10(a), so that the cantilevers bend to contact the sample easily for all of the four cantilevers as shown in Fig. 10(b) even if the tips of four cantilevers are not strictly aligned parallel to the sample surface. The probe is installed in a ultrahigh vacuum chamber equipped with a liquid He tank and reflection-high-energy electron diffraction, in which the electrical conductivity is measured with high surface sensitivity as a function of temperature [45]. The chip is made to approach the sample with three-axis piezo-actuators

σ_x : Conductivity along x
σ_y : Conductivity along y
s : Probe Spacing

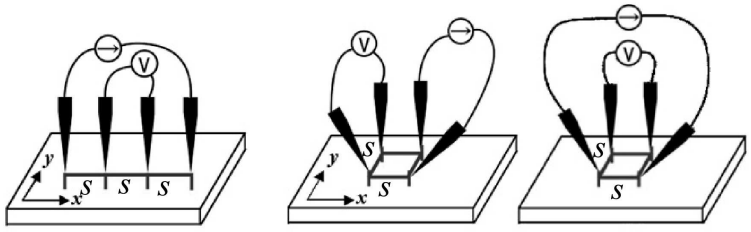

(a) Linear 4PP (b) Square 4PP

Shape of Sample	Linear 4PP		Square 4PP	
	Isotropic	Anisotropic	Isotropic	Anisotropic
3D	$\frac{1}{2\pi\sigma \cdot s}$	$\frac{1}{2\pi\sqrt{\sigma_x\sigma_y} \cdot s}$	$\frac{2-\sqrt{2}}{2\pi\sigma \cdot s}$	$\frac{1}{\pi\sqrt{\sigma_y\sigma_z} \cdot s}\left\{1-\left(1+\frac{\sigma_y}{\sigma_x}\right)^{-\frac{1}{2}}\right\}$
2D	$\frac{\ln 2}{\pi\sigma}$	$\frac{\ln 2}{\pi\sqrt{\sigma_x\sigma_y}}$	$\frac{\ln 2}{2\pi\sigma}$	$\frac{1}{2\pi\sqrt{\sigma_x\sigma_y}}\ln\left(1+\frac{\sigma_y}{\sigma_x}\right)$

FIG. 11: Electrical resistances V/I calculated by solving Poisson's equation for the cases of linear and square four-point-probe methods. The sample is assumed to be isotropic or anisotropic semi-infinite 3D bulk and 2D sheet. The material-specific conductivity σ is the volume conductivity ($\Omega^{-1}\mathrm{cm}^{-1}$) for the 3D specimen and sheet conductivity (Ω^{-1}/Square) for the 2D specimen, respectively; notice that the dimension of the conductivity is different in 3D and 2D.

with a precision of about 50 nm, resulting in gentle contact to the sample surface. Compared with the four-tip STM described above, it is much easier to make the probes contact to the sample, though we cannot change the probe spacing. These two methods, four-tip STM and monolithic μ4PP, are complementary to each other in some aspects.

Since the probe spacing in the μ4PP method is much smaller than the sample size (usually on the order of a millimeter), the sample can be regarded as infinitely large. Then the Poisson equation is solved analytically to calculate the 4PP resistance measured by the μ4PP methods. As shown in Fig. 11, the value of the resistance thus calculated depends on the nature and shape of the sample as well as on the probe spacing and arrangement. There are two kinds of μ4PP methods, a linear μ4PP method, in which the four probes are aligned equidistantly on a line on the sample surface, and a square μ4PP method, in which the four probes are arranged in a square. The sample can be regarded as a semi-infinitely large 3D object when the thickness is much larger than the probe spacing s, while the sample is regarded as a 2D sheet when the thickness is much smaller than s. We can notice two interesting things from the table in Fig. 11:

1. **Probe-spacing dependence**. In the case of 3D samples, the measured value of

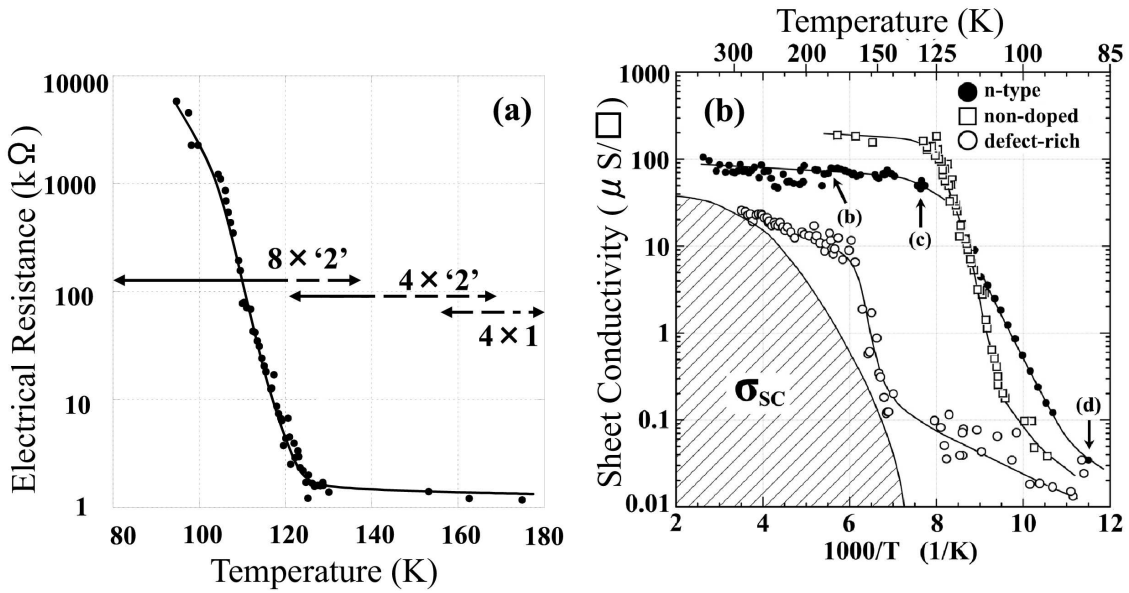

FIG. 12: Temperature dependence of (a) the electrical resistance and (b) the conductivity of Si(111)-4 × 1-In surface [28].

the resistance should be inversely proportional to the probe spacing s, while it does not depend on s for 2D samples. This is true for both the linear 4PP and square-4PP methods, irrespective of the sample being isotropic or anisotropic. This fact is quite useful for distinguishing the current distribution in the sample during the measurement. For example, when the surface layer of a 3D crystal is much more conductive than the underlying bulk region, the measuring current flows mainly in the surface layer. In this case the resistance should be independent of the probe spacing s even though the sample shape is 3D [46]. The other case is semiconductor crystals having a surface inversion layer. The surface layer becomes sometimes an inversion layer in which the majority carrier is different from that in the underlying substrate. Then a *pn* junction is formed between the surface layer and bulk region, which makes the surface layer isolated from the substrate because the junction prevents the measuring current from penetrating deep into the substrate bulk. The measured resistance in this case should also show no probe-spacing dependence, because only the surface layer is measured which is much thinner than the probe spacing. This has actually been demonstrated with a Si(111)-7×7 clean surface and a Si(111)-$\sqrt{3}\times\sqrt{3}$-Ag suface [46]. The former surface shows a $1/s-$dependence of resistance, indicating a 3D distribution of current, while the latter surface shows a $s-$independent character, indicating a 2D distribution of current.

2. **Anisotropic conductivity**. For anisotropic samples, in which the conductivity is

different depending on the directions, the linear 4PP and square-4PP methods provide quite different conclusions. The quasi-1D surfaces such as Si(111)-4×1-In and Si(557)-Au are expected to be highly anisotropic 2D samples, that is, highly conductive along the metal atomic chains while much less conductive in the perpendicular direction. According to the equations in Fig. 11, however, with the linear 4PP method the value of the resistance does not change even if σ_x and σ_y is exchanged. This means that the measured value is the same even when the direction of probe alignment is rotated by 90° with respect to the sample surface. It is easily understood that this is true with any rotation angle. The linear 4PP method provides only the geometrical mean value of σ_x and σ_y. In other words, we cannot obtain the values of σ_x and σ_y separately. On the other hand, as shown by the equations for the square-4PP method in Fig. 11, the resistance value changes by exchanging σ_x and σ_y. Therefore, by changing the combination of current probes and voltage probes in the square arrangement as shown in (b), we obtain two different values of resistance. Then, by solving simultaneous equations using these two values, we can deduce the values of σ_x and σ_y separately. This square-4PP method works very well for the quasi-1D surfaces to obtain the conductivity along the atomic chains as described below [39].

First I discuss the simplest measurements by the linear 4PP method. Figure 12(a) shows the temperature dependence of the resistance of the Si(111)-4×1-In surface measured by the linear μ4PP method with a monolithic μ4PP (Fig. 10) [28]. Though the probe is aligned along the In atomic chains in this measurement, the results do not depend on the probe orientation, as described above. At temperature ranges higher than about 130 K the resistance remains low, while it steeply increases at lower temperature. The electron diffraction patterns observed simultaneously are indicated in the figure; the 4×1 structure changes into the $8 \times' 2'$ structure around 130 K, which correspond to the Peierls transition described in Fig. 7. Therefore, the drastic change in resistance below 130 K is due to a metal-insulator transition caused by the Peierls instability. Figure 12(b) shows the relation between the sheet conductivity (calculated from the measured resistance) and the inverse temperature, together with the data of an n-type Si substrate, a nominally non-doped Si substrate, and a defective surface. The former two surfaces show similar changes in resistance, though the defective surface shows a slightly higher transition temperature. Since at the low-temperature phase the surface is an insulator having an energy gap 2Δ, the temperature dependence of conductivity should be

$$\sigma(T) \propto \exp\left(-\frac{\Delta}{k_B T}\right). \tag{5}$$

Therefore, by fitting the data points at the lowest temperature region in Fig. 12(b), the energy gap is determined to be $2\Delta \simeq 200 \sim 300$ meV, which is similar to that estimated by photoemission spectroscopy [27]. The hatched area in Fig. 12(b) indicates the conductivity σ_{SC} through the surface space-charge layer beneath the surface, which is calculated by using the information about band bending and the resulting excess carrier concentration, and also the temperature dependence of the carrier mobility. Since the carrier concentration

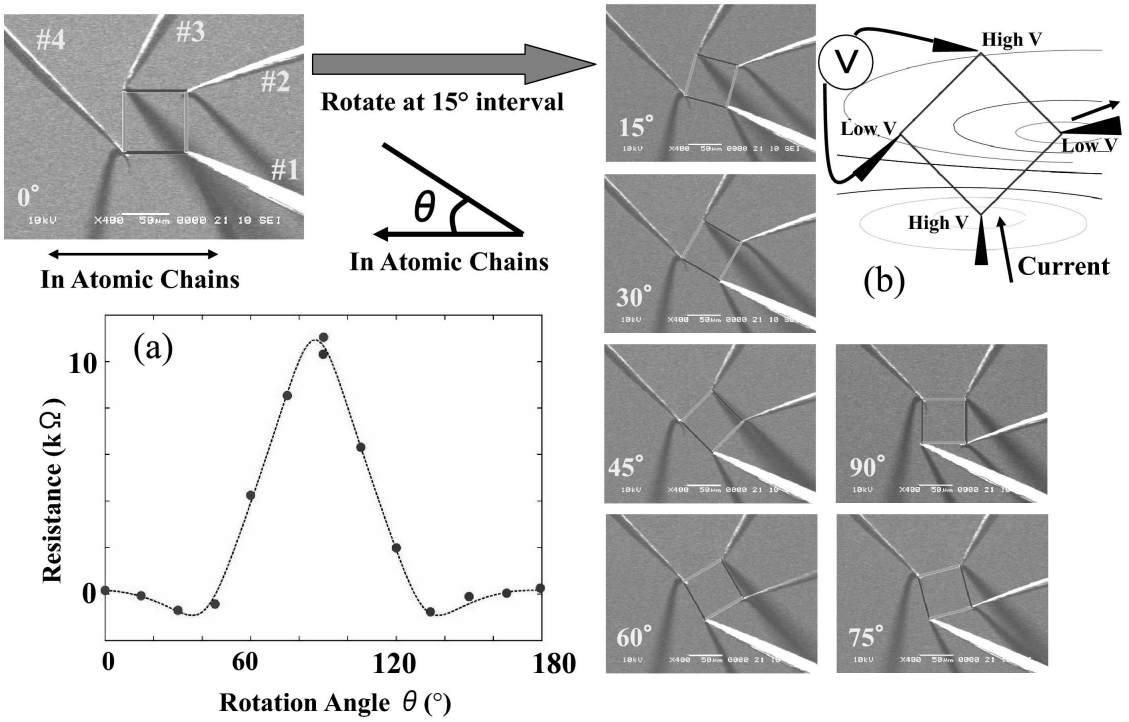

FIG. 13: Resistance of the single-domain Si(111)-4 × 1-In surface measured by the rotational square-4PP method using a four-tip STM [39]. As shown by SEM images, the four tips are arranged in a square with a side of 60 μm on the sample surface, and the square is rotated at 15° intervals with respect to the sample surface. (a) The resistance is measured at each angle with two combinations of current and voltage probes. The data points are fitted by Eq. (6). (b) A distribution of equi-potential lines calculated by assuming $\sigma_x/\sigma_y = 20$. It shows that the apparent resistance measured at $\theta = 135°$ is negative.

in the surface space-charge layer is rapidly frozen out below about 150 K, σ_{SC} drops steeply and becomes much smaller than the measured conductivity. This means that the measured conductivity, especially below 150 K, is the surface-state conductivity, not a conductivity through the Si substrate. Thus a metal-insulator transition in surface electronic states is clearly observed as a change in conductivity.

Next the measurement of the anisotropic conductivity is discussed for Si(111)-4 × 1-In. As mentioned before, the square-μ4PP method is effective for this. The actual measurements involve not only exchanging the combination of current and voltage probes as shown in Fig. 11(b), but also rotating the square with respect to the sample surface as shown by the SEM images in Fig. 13. At each rotation angle θ, the measurement is done by two combinations of the current and voltage probes. As shown by the data points in Fig. 13(a), the apparent resistance thus measured changes significantly with the rotation angle of the square. If the sample is isotropic, the measured resistance should be constant.

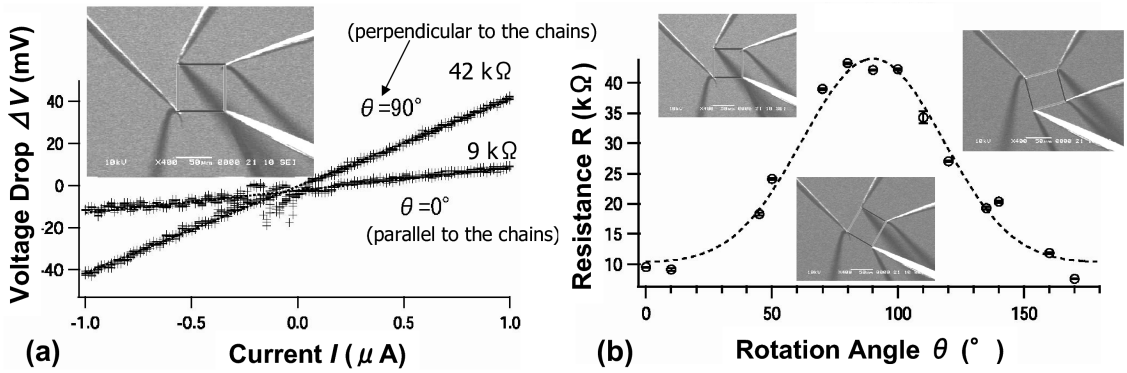

FIG. 14: (a) Current-Voltage characteristics measured by the square-4PP method. $\theta = 0°$ corresponds to the configuration where the current flows and the voltage is measured along the Au chains. $\theta = 90°$ corresponds to a measurement in the perpendicular direction. (b) Resistance of the Si(557)-Au surface, measured as a function of the rotation angle θ in the square-4PP method. The probe spacing (side of the probe square) was 75 μm. Insets are SEM images of the probes contacting the sample surface. The Au chains run along the $[10\bar{1}]$ direction (horizontal direction in these images) [47].

As shown by the dotted line in Fig. 13(a), the result is well fitted by

$$\frac{V}{I} = \frac{1}{2\pi\sqrt{\sigma_x\sigma_y}} \cdot \ln \sqrt{\frac{(\sigma_x/\sigma_y + 1)^2 - 4\cos^2\theta \sin^2\theta(\sigma_x/\sigma_y - 1)^2}{(\sin^2\theta + \sigma_x/\sigma_y \cos^2\theta)^2}}, \tag{6}$$

which is obtained by solving Poisson's equation for an anisotropic 2D sheet having a conductivity σ_x along the x-direction and σ_y along the y-direction. From this fitting, the values of σ_x (along the In atomic chains) and σ_y (across the chains) are obtained separately:

$$\sigma_x = 7.1 \times 10^{-4} \quad (\Omega^{-1}/\text{Square}), \tag{7}$$

$$\sigma_y = 1.3 \times 10^{-5} \quad (\Omega^{-1}/\text{Square}). \tag{8}$$

The ratio σ_x/σ_y is as high as 54, meaning that the conductivity along the In atomic chains is much higher than in the perpendicular direction. Figure 13(b) shows a distribution of equi-potential lines calculated by assuming $\sigma_x/\sigma_y = 20$. The distribution is significantly distorted due the anisotropy, so that at some rotation angle θ the measured voltage is negative. This shows that the apparent resistance measured at $\theta = 135°$ is negative.

Let us check whether this high anisotropy in surface conductivity is reasonable or not by comparing the anisotropic surface-state bands in Fig. 6. The conductivity can be calculated from the band dispersion by using the Boltzmann equation,

$$\sigma_{ij} = \frac{e^2}{2\pi^2\hbar} \int \tau_k \frac{v_{ki} v_{kj}}{\mid v_k \mid} dk_{\mathrm{F}}\,, \tag{9}$$

for 2D systems, where τ_k is the carrier relaxation time. Here the group velocity v_{ki} in the ith direction at the Fermi level is given by the band dispersion, $v_{ki} = 1/\hbar \cdot \partial E/\partial k_i$. The integral is done along the Fermi lines. Since the surface has three metallic bands, m1, m2, and m3, as shown in Fig. 6, the contribution from each band should be summed up. Then the conductivity tensor is, in units of 10^{10} S/Square,

$$\begin{pmatrix} \sigma_{xx} & \sigma_{xy} \\ \sigma_{yx} & \sigma_{yy} \end{pmatrix} = \begin{pmatrix} 6.2\tau_x & 0 \\ 0 & 0.34\tau_y \end{pmatrix} + \begin{pmatrix} 6.1\tau_x & 0 \\ 0 & 0 \end{pmatrix} + \begin{pmatrix} 1.2\tau_x & 0 \\ 0 & 0.38\tau_y \end{pmatrix}. \tag{10}$$

Here τ_x and τ_y are the carrier relaxation times in the direction of the In atomic chains and in the perpendicular direction, respectively, which are unknown parameters. Then the conductivities in the respective directions are

$$\begin{aligned} \sigma_x &= \sigma_{xx} = 1.4 \times 10^{11}\tau_x, \\ \sigma_y &= \sigma_{yy} = 7.2 \times 10^{9}\tau_y. \end{aligned} \tag{11}$$

By assuming that this σ_x is equal to the value in Eq. (7), the relaxation time is obtained, $\tau_x \sim 5 \times 10^{-15}$ sec. Furthermore, by multiplying this value of τ_x with the Fermi velocity $v_F = \hbar k_F/m^*$ that is calculated from the band dispersion, the carrier mean free path $\ell = v_F\tau_x$ is estimated to be $\ell \sim 3$ nm. The carriers flow along the In atomic chains with this mean free path, which is one order of magnitude shorter than in a bulky In crystal at room temperature but much larger than the lattice constant. This means that the carrier scattering by phonons and defects is much more frequent in the atomic chains than in the 3D crystal, but the carriers can propagate without scattering over a distance ten times longer than the lattice constant. On the other hand, as a crude approximation, if $\tau_x = \tau_y$ is assumed in Eq. (11), the ratio σ_x/σ_y is about 20, which agrees reasonably with the measured value $\sigma_x/\sigma_y \sim 54$ in spite of the crude assumption. This means the observed anisotropy in surface conductivity surely comes from the surface-state bands. Inversely, if we assume the experimental ratio $\sigma_x/\sigma_y \sim 54$, we obtain $\tau_x/\tau_y \sim 3$ from Eq. (11). This means that carriers flow along the In atomic chains with a much longer relaxation time than in the perpendicular direction, which is also a natural consequence of quasi-1D metallic surfaces.

In this way, the measured surface conductivity is explained by the Boltzmann equation combined with the surface-state band structure for the case of Si(111)-4 × 1-In. This is a case of a 'clean metal' surface, in which the carriers propagate as a wave coherently over a distance much longer than the lattice distance. However the next example of a quasi-1D metallic surface, Si(557)-Au, shows a different behavior, which is that of a 'bad metal' surface, although the band dispersion is quite similar to that of the Si(111)-4 × 1-In. This is due to a much higher density of defects on the Si(557)-Au.

Figure 14 shows the results of square-4PP measurements of the Si(557)-Au surface at room temperature with the four-tip STM [47]. It actually shows different resistance values between along the Au chains and in the perpendicular direction. The conductivity along the Au chains (σ_x) and that in the perpendicular direction (σ_y) are $\sigma_x = 9.3 \times 10^{-6}$ S/Square and $\sigma_y = 3.5 \times 10^{-6}$ S/Square, respectively. The ratio between them is $\sigma_x/\sigma_y \sim 3$,

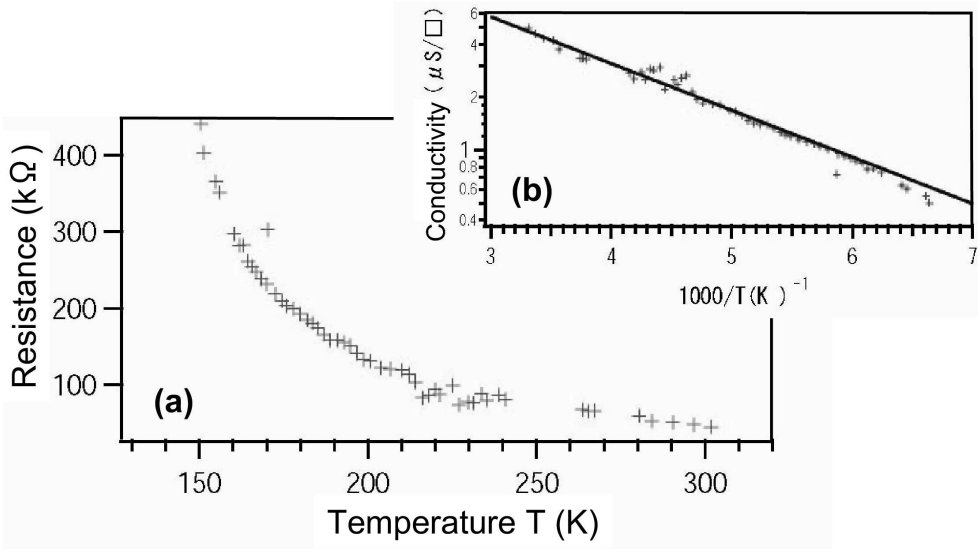

FIG. 15: (a) The 4PP-resistance and (b) surface conductivity of the Si(557)-Au surface, measured by the variable-temperature monolithic μ4PP method. The 20 μm-spacing probes were aligned along the Au chains [47].

which is much smaller than that of the Si(111)-4 × 1-In surface mentioned above. Next, similar to the case of 4 × 1-In, the conductivity is calculated by assuming the Boltzmann picture, Eq. (9) with the known Fermi surface and band dispersion (as shown in Fig. 8(a)), $\sigma_x = 1.3 \times 10^{11} \times \tau_x$ S/Square. Next, by assuming this result to be equal to the measured value of σ_x, we obtain the carrier relaxation time $\tau_x \sim 7 \times 10^{-17}$ sec. Then, by multiplying this value with the Fermi velocity, the carrier mean free path is obtained, $\ell \sim 0.6$ Å. Since, however, this mean free path value is much smaller than the lattice constant, the analysis does not make sense. In other words, the Boltzmann picture is not applicable for the transport mechanism along the Au chains; the carriers do not propagate as a wave.

Next we measured the temperature dependence of the resistance of the Si(557)-Au surface by the monolithic μ4PP method. As shown in Fig. 15(a), the resistance increases as the temperature is lowered. By taking the inverse of the resistance and plotting it as a function of the inverse temperature, as shown in (b), the conductivity is found to exponentially decrease with cooling below room temperature, indicating a nonmetallic conduction. This conclusion is the same as in the previous study [48]. The data points are well fitted by $\sigma \propto \exp[-\Delta/k_B T]$, giving an energy gap $2\Delta = 110$ meV. This non-metallic behavior contradicts the PES result in Fig. 8, that the Si(557)-Au surface has a metallic band at room temperature.

What is the nature of electrical conduction along the Au chains? Recalling the dense and irregular bright protrusions on the Au chains in the STM image of Fig. 3(b), which are assigned to be extra Si adatoms [32], they seem to break the metallic chains into separated

segments. In such a case, the conduction is described in terms of variable-range hopping (VRH) [49]. In the temperature range in Fig. 15, the theory of VRH shows that the conductivity is an activation-type hopping conduction ($\sigma \propto \exp[-\Delta/k_BT]$). In the case of the Si(111)-4×1-In surface at the high-temperature metallic phase, for comparison, no such irregularities exist on the chains (Fig. 2(a)), so that the Boltzmann picture is quantitatively applicable and the surface shows metallic transport. The dense protrusions can alter the band structure itself locally to be semiconducting. It is known for the Si(111)5×2-Au surface that similar protrusions change the metallic chains into semiconducting chains locally, due to electron doping [50, 51]. The same thing may happen on the Si(557)-Au surface, which divides the Au chains into metallic regions and semiconducting regions, so that the transport property shows semiconductivity while the photoemission shows a metallic character.

Thus, atomic-scale irregularities such as protrusions composed of adatoms or clusters can cause a decisive influence on the transport properties of quasi-1D systems. The carriers there cannot avoid them and interact with the defects in the most effective way.

So far I have described the cases of quasi-1D surface superstructures composed of massive arrays of metal atomic chains. The chains are so close to each other that there is finite inter-chain coupling. The current for measuring the conductivity flows not only along the chains but also spreads laterally across the chains. So the system can be considered as a highly anisotropic 2D metal rather than a quasi-1D metal. The measured conductivity is the sheet conductivity, not a conductivity of individual chains (though we can estimate the conductivity of each chain from the sheet conductivity along the chain direction, σ_x).

The final example is Co-silicide nanowires which are well separated from each other (Fig. 4), so that we can measure the conductivity of individual wires. As shown in Fig. 16(a), the four STM tips are brought into direct contact with a $CoSi_2$ nanowire formed on a Si(110) surface in UHV-SEM, and the 4PP resistance is measured [52]. Recently metal-coated carbon nanotube (CNT) STM tips were developed, as shown in (c) [53–55]. Since the diameter of the CNT tip is much smaller than the W tips, the spacing between the tips can be greatly reduced, as shown in Figs. 16(b)(e)-(i) [55], down to about 20 nm. The CNT tip is so flexible that the contact is very gentle without creating significant damage on the sample surface (as well as at the end of the tip). Figure 16(d) shows the 4PP resistance measured as a function of the spacing between the voltage probes (tip 2 and tip 3). The resistance is linearly proportional to the spacing down to 20 nm. This means that the transport is diffusive, obeying Ohm's law. The gradient of the straight line gives a 1D resistivity $\rho_{1D} = 57 \pm 3\ \Omega/\mu$m. By extrapolating the data points, there seems to be no residual resistance at zero probe spacing, which is owing to the four-point probe configuration. The linear relation between the resistance and the probe spacing means another important thing, that is, no leakage of current to the 3D substrate or to the 2D substrate surface. This is because a Schottky barrier between the nanowire and the Si substrate confines the current in the nanowire only [52]. The mean free path of the electrons in $CoSi_2$ is around 6 nm at room temperature [56],which is much smaller than the width and height of our nanowire as well as the probe spacing. Therefore, our result for diffusive conduction is reasonable. From the 1D resistivity ρ_{1D} and the cross section of the wire, the 3D resistivity is obtained to be about 20 $\mu\Omega$·cm, which is similar to the

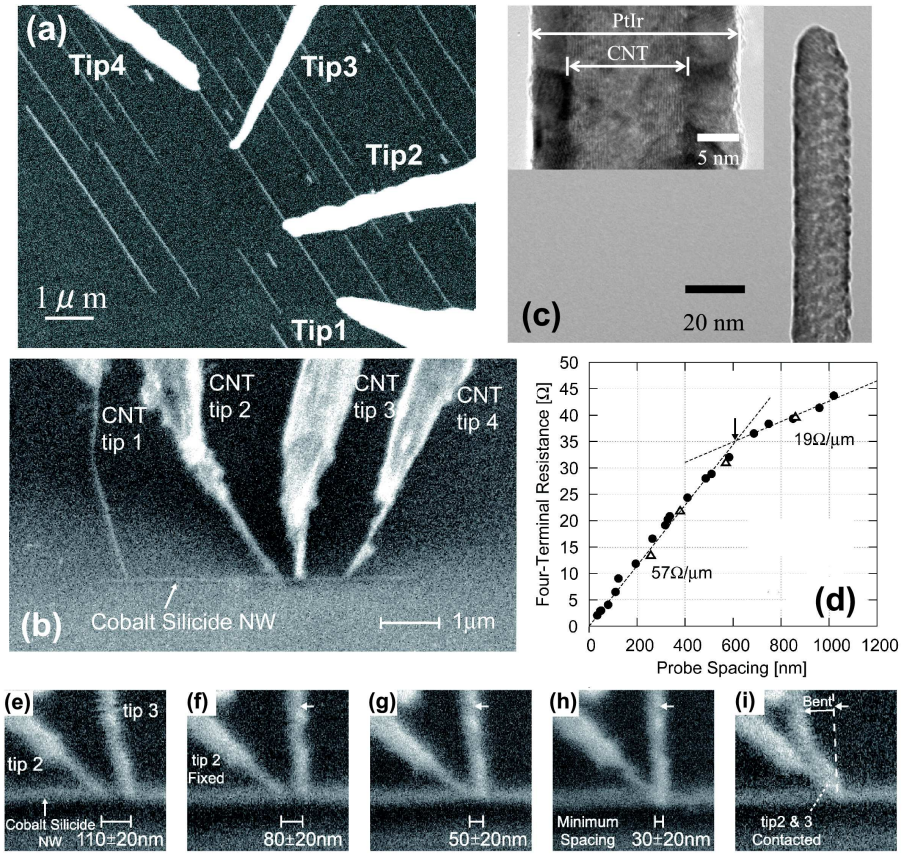

FIG. 16: The 4PP measurements of $CoSi_2$ nanowires. (a) A SEM image of the four W tips contacting a nanowire. The current passed through the tips 1 and 4, and the voltage drop was measured between the tips 2 and 3 [52]. (b) A SEM image of the four PtIr-coated carbon nanotube tips contacting a nanowire [55]. (c) A TEM image of a PtIr-coated CNT tip. The inset shows the magnified image [60]. (d) Plot of 4PP resistance vs. the spacing between the voltage probes [55]. The arrow around 600 nm in the graph indicates the position where the NW width changes, resulting in a change of the resistivity. No difference is found between before and after the physical contacts of the CNT tip 3 on the NW (see circles and triangles in the graph). (e)-(i) SEM images of the voltage probes (tips 2 and 3) at different spacings. The current probes (tips 1, 4) are about 1 μm away from these voltage probes (see (b)). (i) The voltage probes contacted each other, and the CNT tip 3 was bent. (h) The minimum probe spacing before the contact is 20 $\sim$ 30 nm. The error bar in the probe spacing is determined by the radii of the apexes in tips 2 and 3 [55].

value for an epitaxy-grown $CoSi_2$ thin film [57]. In the ballistic transport regime, 2PP and 4PP resistances do not depend on the probe spacing [58]. They depend only on the total transmission probability of the electron wavefunction between the voltage probes, tip 2 and tip 3. By cooling the sample to elongate the mean free path of carriers (ca. 100 nm at 4 K [57]), such ballistic transport phenomenon can be observed by the four-tip STM operated

at low temperature [40]. It should be noted here that, when one measures the resistance with the 2PP method, the contact resistance between the probes and sample hampers the measurements of sample resistance. Actually in the present case of $CoSi_2$ nanowire and PtIr-coated CNT tips, the contact resistance at each contact point could not be less than 50 kΩ, which is much larger than the sample resistance (a few Ω at the probe spacing of 50 nm). The contact resistance cannot be reduced below this value because of the very small contact area. In this sense the 4PP configuration is indispensable.

V. CONCLUDING REMARKS

I have introduced several examples of surface-1D structures, their band dispersions, Fermi surfaces, and transport properties. The results presented here clearly indicate that the electrical conduction through atomic chains and nanowires on silicon surfaces are actually measurable quantitatively. During the investigation, we have noticed several important things: (1) The probe-spacing dependence of 4PP resistance is useful for distinguishing the dimensionality of the measured region. (2) The square-4PP method is effective for measuring anisotropic conductivity. (3) The μ4PP methods are very surface-sensitive and convenient for obtaining the analytical solution in theory.

We have also learned that atomic-scale point defects such as adatoms and small clusters affect the transport properties decisively, especially in the 1D systems. It was also shown (in a 2D metallic surface superstructure) that surface line defects such as steps also influence the electrical conduction at surfaces [4]. However, the interaction between the defects and surface-state carriers is expected to provide interesting effects which are much more enhanced compared with in the 3D bulk. For example, the Kondo effect and RKKY interaction with magnetic impurities can be enhanced in the strict 2D and quasi-1D systems on crystal surfaces.

These achievements are an important starting point for exploring quantum transport properties characteristic to the surface-1D structures. Since the minimum probe spacing in the four-tip STM is around $20 \sim 30$ nm, which is larger than the mean free path of carriers at room temperature (a few nm), but comparable to that at low temperatures (~ 100 nm at liquid He temperature), the measurements by a low-temperature four-tip STM are required to detect the quantum transport phenomena. Measurements under a magnetic field are also expected to provide various interesting information on the transport. In addition to the measurement methods, more interesting samples are required which have well-controlled structures at atomic scales as well as on a mesoscopic scale. For example, intentional carrier doping into the surface-1D structures is quite interesting for tuning the band filling, electron-phonon, and electron-electron interactions. Control of the domain shapes of the surface-1D structures is also important, not only for observing the fundamental physical phenomena such as the quantum spin Hall effect, but also for applications to electronic devices. Sample fabrication techniques should also be improved by using, e.g., focus-ion-beam deposition and dip-pen methods in addition to the usual micro-fabrication methods in semiconductor technology. Looking for materials for fabricating the 1D structures is

also an interesting subject, including molecules and supra-molecules [59]. Compared with the 1D systems made of the 2DEG at semiconductor hetero-junctions, the study of surface 1D systems is still in its infancy, and, therefore, offers much more room for exploring new physics.

Acknowledgements

I gratefully acknowledge the present and former members of my research group in The University of Tokyo; many of them have greatly contributed to the construction of the four-tip STM and monolithic μ4PP apparatuses, and their applications to various samples. I also acknowledge the collaboration with Prof. Mitsuhiro Katayama's group in Osaka University on the metal-coated carbon nanotube tips and also with UNISOKU Co. Ltd. for constructing the apparatuses. This work has been supported in part by Grants-In-Aid from the Japanese Society for the Promotion of Science. I have been supported also by the SENTAN Project (Development of System and Technology for Advanced Measurement and Analysis) of the Japan Science and Technology Agency (JST).

References

* Electronic address: shuji@surface.phys.s.u-tokyo.ac.jp
[1] A. Kawabata, Rep. Prog. Phys. **70**, 219 (2007).
[2] J. H. Davies, *The Physics of Low -Dimensional Semiconductors* (Cambridge University Press, Cambridge, England, 1998).
[3] R. Landauer, IBM J. Rev. Dev. **1**, 223 (1957).
[4] I. Matsuda *et al.*, Phys. Rev. Lett. **93**, 236801 (2004).
[5] H. Sakaki, Jpn. J. Appl. Phys. **19**, L735 (1980).
[6] G. Grüner, *Density waves in solids*, Addison-Wesley, 1994 New York.
[7] H. Ishii *et al*, Nature **426**, 540 (2003).
[8] M. Bockrath *et al.*, Nature **397**, 598 (1999).
[9] P. Gambardella *et al.*, Nature **416**, 301 (2002).
[10] S. Tarucha, T. Honda, and T. Saku, Solid State Commun. **94**, 413 (1995).
[11] O. Bunk *et al.*, Phys. Rev. B **59**, 12228 (1999).
[12] S. Mizuno, Y. O. Mizuno, and H. Tochihara, Phys. Rev. B **67**, 195410 (2003).
[13] T. Abukawa, T. Yamazaki, and S. Kono, e-J. Surf. Sci. Nanotech. **4**, 661 (2006).
[14] J. Nakamura, S. Watanabe, and M. Aono, Phys. Rev. B **63** 193307 (2001).
[15] J.-H. Cho, D.-H. Oh, K. S. Kim, and L. Kleinman, Phys. Rev. B **64** 235302 (2001).
[16] For a review see, S. Hasegawa *et al.*, Jpn. J. Appl. Phys. **39**, 3815 (2000).
[17] S. Hasegawa, X. Tong, S. Takeda, N. Sato, and T. Nagao, Prog. Surf. Sci. **60**, 89(1999).
[18] H. Okino, I. Matsuda, T. Tanikawa, and S. Hasegawa, e-J. Surf. Sci. Nanotech. **1**, 84 (2003).
[19] I. K. Robinson, P. A. Bennett, and F. J. Himpsel, Phys. Rev. Lett. **88**, 096104 (2002).
[20] J. Nogami, B. Z. Liu, M. V. Katkov, C. Ohbuchi, and N. O. Birge, Phys. Rev. B **63**, 233305 (2001).
[21] Z. He, M. Stevens, D. J. Smith, and P. A. Bennett, Appl. Phys. Lett. **83**,5292 (2003); Surf.

Sci. **524**, 148 (2003); J. Appl. Phys. **93**,5670 (2003).
[22] Z. He, D. J. Smith, and P. A. Bennett, Phys. Rev. Lett. **93**,256102 (2004); Phys. Rev. B **70**, 241402 (2004).
[23] M. M. R. Evans and J. Nogami, Phys. Rev. B **59**, 7644 (1999).
[24] H. Morikawa, I. Matsuda, and S. Hasegawa, Hyomen Kagaku **25**, 407 (2004) [in Japanese].
[25] T. Abukawa *et al.*, Surf. Sci. **325**, 33 (1995).
[26] H. W. Yeom *et al.*, Phys. Rev. Lett. **82**, 4898 (1999).
[27] H. W. Yeom, K. Horikoshi, H. M. Zhang, K. Ono, and R. I. G. Uhrberg, Phys. Rev. B **65**, 251307(R) (2002); J. R. Ahn *et al.*, Phys. Rev. Lett. **93**, 106401 (2004).
[28] T. Tanikawa, I. Matsuda, T. Kanagawa, and S. Hasegawa, Phys. Rev. Lett. **93**, 016801 (2004).
[29] H. W. Yeom, Phys. Rev. Lett. **97**,189701 (2006).
[30] C. González, F. Flores, and J. Ortega, Phys. Rev. Lett. **97**,189702 (2006).
[31] C. González, F. Flores, and J. Ortega, Phys. Rev. Lett. **96**, 136101 (2006).
[32] K. N. Altmann *et al.*, Phys. Rev. B **64**, 035406 (2001); J. N. Crain *et al.*, Phys. Rev. B **69**, 125401 (2004); J. N. Crain, K. N. Altmann, C. Bromberger, and F. J. Himpsel, Phys. Rev. B **66**, 205302 (2002).
[33] J. R. Ahn, H. W. Yeom, H. S. Yoon, and I. W. Lyo, Phys. Rev. Lett. **91**, 196403 (2003)
[34] I. Barke, F. Zheng, T. K. Rugheimer, and F. J. Himpsel, Phys. Rev. Lett. **97**, 226405 (2006).
[35] P. Segovia, D. Purdie, M. Hengsberger, and Y. Baer, Nature **402**, 504 (1999); O. Gallus, Th. Pillo, M. Hengsberger, P. Segovia, and Y. Baer, Eur. Phys. J. B, **20**, 313 (2001).
[36] R. Losio *et al.*, Phys. Rev. Lett. **86**, 4632 (2001).
[37] I. Shiraki, F. Tanabe, R. Hobara, T. Nagao, and S. Hasegawa, Surf. Sci. **493**, 643 (2001).
[38] S. Hasegawa, I. Shiraki, F. Tanabe, and R. Hobara, Current Appl. Phys. **2**, 465 (2002).
[39] T. Kanagawa *et al.*, Phys. Rev. Lett. **91**, 036805 (2003).
[40] R. Hobara *et al.*, Rev. Sci. Instr., 78, 053705(2007).
[41] R. Hobara, S. Hasegawa, and T. Nagamura, Japanese Patent, submitted (2007).
[42] H. Okamoto and D. M. Chen, J. Vac. Sci. Technol. A **19**, 1822 (2001).
[43] C. L. Petersen, F. Grey, I. Shiraki, and S. Hasegawa, Appl. Phys. Lett. **77**, 3782 (2000); I. Shiraki *et al.*, Surf. Rev.Lett. **7**, 533 (2000); P. Boggild *et al.*, Rev. Sci. Instrum. **71**, 2781 (2000); T. M. Hansen *et al.*, Rev. Sci. Inst. **74**, 3701 (2003).
[44] http://www.capres.com.
[45] T. Tanikawa, I. Matsuda, R. Hobara, and S. Hasegawa, e-J. Surf. Sci. Nanotech. **1**, 50 (2003).
[46] S. Hasegawa *et al.*, Surf. Rev. Lett. **10**, 963 (2003); S. Hasegawa, J. Phys.: Cond. Matters **12**, R463 (2000); S. Hasegawa and F. Grey, Surf. Sci. **500**, 84 (2002); S. Hasegawa *et al.*, J. Phys.: Cond. Matters **14**, 8379 (2002).
[47] H. Okino *et al.*, Phys. Rev. **70**, 113404 (2004).
[48] M. Schöck, C. Sürgers, and H. v. Löhneysen, Thin Solid Films **428**, 11 (2003).
[49] M. M. Fogler, S. Teber and B. I. Shklovskii, Phys. Rev. B **69**, 035413 (2004).
[50] S. C. Erwin, Phys. Rev. Lett. **91**, 206101 (2003).
[51] H. S. Yoon, S. J. Park, J. E. Lee, C. N. Whang, and I.-W. Lyo, Phys. Rev. Lett. 92, 096801 (2004).
[52] H. Okino *et al.*, Appl. Phys. Lett. **86**, 233108 (2005).
[53] T. Ikuno *et al.*, Jpn. J. Appl. Phys. **43**, L644 (2004).
[54] Y. Murata *et al.*, Jpn. J. Appl. Phys. **44**, 5336 (2005); S. Yoshimoto *et al.*, Jpn. J. Appl. Phys. **44**, L1563 (2005).
[55] S. Yoshimoto *et al.*, Nano Letters **4**, 956 (2007).
[56] P. B. Allen and W. W. Schulz, Phys. Rev. B **47**, 14434 (1993).
[57] J. C. Hensel, R. T. Tung, J. M. Poate, and F. C. Unterwald, Phys. Rev. Lett. **54**, 1840 (1985).

[58] S. Datta, *Electronic Transport in Mesoscopic Systems* (Cambridge University Press, Cambridge, England, 2002).
[59] T. Yokoyama, S. Yokoyama, T. Kamikado, Y. Okuno, and S. Mashiko, Nature **413**, 619 (2001).
[60] H. Konishi *et al.*, Rev. Sci. Instr. **78**, 013703 (2007).